TECHNICAL NOTE

Coupled modeling and numerical simulation of gas flows laden with solid particles in de Laval nozzles

L. Zhang[1] · Q. Yu[1] · T. Liu[1] · Z. Feng[1] · M. Sun[1] · H. Jin[1]

Abstract

Supersonic gas–solid separation is a new dedusting concept, in which a de Laval nozzle is employed to accelerate a gas laden with solid particles to supersonic speeds. In the present work, a correction for the curved nature of the nozzle walls is implemented in the turbulent boundary layer model. A gas-particle coupled quasi-one-dimensional flow model is established based on an Eulerian–Lagrangian method. Combining the flux vector splitting of gas-phase equations, fifth-order weighted essentially non-oscillatory spatial discretization, and three-step third-order total variation diminishing Runge–Kutta time marching, we create a set of uniformly high-order accurate, stable, and efficient numerical methods. The validation against previous experiments demonstrates the validity and accuracy of the numerical model. The dependence of the flow fields on parameters including particle size and mass loading, nozzle inlet stagnation temperature and pressure, and nozzle expansion angle is numerically computed and analyzed. The results show that the decrease in particle size or mass loading and the increase in inlet stagnation temperature, pressure, or nozzle expansion angle facilitate an increase in exit particle velocity. The increase in particle size, inlet stagnation pressure, or nozzle expansion angle and the decrease in particle mass loading or inlet stagnation temperature increase the exit gas Mach number. In the current parametric study, particle size and mass loading have the largest effects on exit particle velocity and exit gas Mach number, respectively.

Keywords De Laval nozzle · Dedusting · Turbulent boundary layer model · Quasi-one-dimensional · Eulerian–Lagrangian method

List of symbols

A	Cross-sectional area
a	Local sound speed
a^{gp}	Drag force of gas flow per unit particle mass
B	Width
B_{e}	Exit height
B_{i}	Inlet height
B_{t}	Throat height
C_1	Constant in the turbulent boundary layer model
C_2	Constant in the turbulent boundary layer model
C_3	Constant in the turbulent boundary layer model
C_{D}	Drag coefficient
C_{f}	Wall friction coefficient
C_{h}	Stanton number
c_{p}	Particle specific heat
c_{pg}	Specific heat of a gas at constant pressure
D	Local equivalent diameter of the wetted perimeter
d_{p}	Particle diameter
E_{r}	Residual
E_{rp}	Relative error function of pressure
e	Specific internal energy
e^*	Specific total energy
$\mathbf{F}$	Flux vector
f^{gp}	Drag force of gas flow on a particle
f^{pp}	Collision force between particles
f_{wf}	Wall friction
G^{gp}	Rate of work on a particle caused by gas flow force

1 School of Mechanical Engineering and Automation, Zhejiang Sci-Tech University, Hangzhou 310018, China

G^{pg}	Cell-volume averaged rate of work from particles to the gas
G_{w}	Frictional rate of work by walls per unit cell volume
g	Gravitational acceleration
h_{g}	Static specific enthalpy of the gas
h_{g0}	Stagnation specific enthalpy of the gas
h_{w}	Wall enthalpy
J	Maximum node or cell number
JI	Cell number in which particle i resides
$\mathrm{Kn_p}$	Particle Knudsen number
L_1	Length of the convergent section
L_2	Length of the divergent section
M_{g}	Gas Mach number
M_{p}	Particle Mach number
$M_{\mathrm{p,cr}}$	Critical particle Mach number
m^{p}	Mass of a single particle
N_{cp}	Number of physical particles represented by a computational particle
N_{inj}	Computational particle number injected every time step
N_{JI}	Total number of particles in cell j where particle i resides
Nu	Nusselt number
Pr	Prandtl number
p	Static pressure
$p_{\mathrm{c}i}$	Computational pressure at measurement point i
$p_{\mathrm{m}i}$	Measured pressure at measurement point i
P_{s}	Constant in the collision force model
Q^{gp}	Heat transfer rate from the gas to a particle
Q^{pg}	Cell-volume averaged heat transfer rate from particles to the gas
Q_{w}	Heat transfer rate from walls per unit cell volume
q_{mg}	Gas mass flow rate
q_{mp}	Particle mass flow rate
R	Gas constant
R_0	Transition arc radius
$\mathrm{Re_p}$	Particle Reynolds number
Re_x	Reynolds number at x position
$\mathbf{S}$	Source vector
T_{g}	Gas temperature
T_{p}	Particle temperature
T_{w}	Wall temperature
t	Time
$\mathbf{U}$	Primitive vector of solution
V_{cell}	Grid cell volume
V_{p}	Volume of a single particle
v_{g}	Gas velocity
v_{p}	Particle velocity
x	Position along the nozzle axis
x_{p}	Particle position

α	Volume fraction of gas phase
β	Constant in the collision force model
γ	Ratio of specific heats of the gas
Δt	Time step
Δx	Spatial step
δ	Nozzle expansion angle
ε_{r}	Threshold value of residual
ζ	Boundary layer correction factor
μ	Dynamic viscosity of the gas
ρ_{g}	Density of the gas
ρ_{p}	Particle density
τ_{v}	Velocity relaxation time
φ	Particle volume fraction
φ_{c}	Particle volume fraction at close packing
φ_i	Local particle volume fraction in the grid cell where particle i resides
ψ	Particle mass loading

1 Introduction

Supersonic gas–solid separation dedusting technique is a relatively new concept that was first proposed by Xu et al. [1]. This technique usually utilizes two de Laval (or convergent–divergent) nozzles with rectangular cross sections to accelerate a particle-laden gas and clean air (or steam) to supersonic speeds. An oblique shock wave is created exactly at each nozzle exit (see lines AC and AD in Fig. 1). In order to accomplish this, one must match the exit gas Mach numbers (M_{g1} and M_{g2}) and the angles between the nozzle walls (EA and FA) and the interface (AB), whose supplementary angles are termed separation angles. If both the nozzle-exit particle velocity and the upper separation angle are large enough, an inertial separation of the gaseous and particulate phases is able to be achieved through the oblique shock wave AC. Subsequently, these solid particles are taken away by another air (or steam) flow. Both the cleaned gas and the dusty air (or steam) move forward and leave this separation equipment through respective ducts. This dedusting concept was proposed to resolve the problem of dedusting high-pressure high-temperature gases in coal-fired advanced combined cycle systems such as integrated gasification combined cycles and pressurized fluidized bed combustion combined cycles [2]. In such applications, in order to insure the safety of the gas turbines and to meet the environment protection requirements for exhausted gases, solid particles with diameters of greater than 5 μm are required to be adequately accelerated in the nozzle and thus ultimately separated.

The ability to ensure separation of these dust particles primarily depends on an accurate understanding of the flow behavior within the nozzle, such as the dependence of the flow field on parameters including particle size and mass
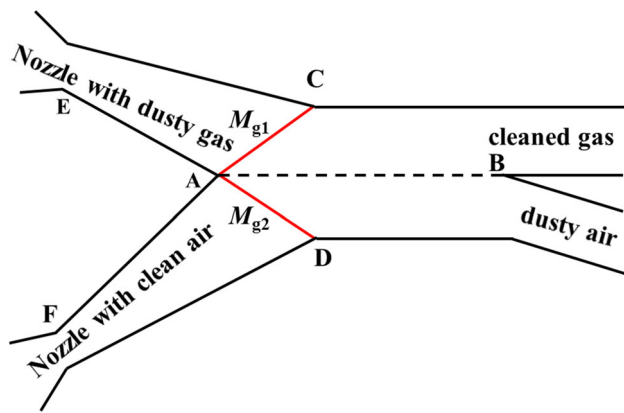
Fig. 1 Schematic of dedusting technique by supersonic gas–solid separation

loading, nozzle-inlet stagnation temperature and pressure, and nozzle expansion angle. These parameters are crucial to the optimum design and operation under design or off-design conditions. Therefore, we only focus on the particle-laden gas flow in the de Laval nozzle in this study. The exit particle velocity and gas Mach number are two other crucial parameters determining the dedusting efficacy. The separation angle is the final crucial parameter, but is outside of this study. Moreover, the local particle volume fraction determines the interphase coupling. The variations in the nozzle of these parameters will be analyzed due to their significant importance.

In spite of a large number of two- or three-dimensional modeling and computational methods for studying nozzle gas-particle flows [3–6], one-dimensional methods are widely used for the analysis of relationships between parameters derived from experiments or computations, and for the design of nozzles due to their simplicity, clarity, and validity. Thus, our present pursuit is to establish a quasi-one-dimensional nozzle flow prediction model suited for supersonic gas–solid separation. Eulerian–Eulerian (EE or two-fluid) methods contain inherent limitations related to particle Stokes number and the assumption of unique field representations for particle velocity and temperature [7, 8]. Therefore, the Eulerian–Lagrangian (EL or trajectory) approach is adopted in the present modeling. During the modeling process, we will encounter crucial challenges in the following four aspects. In the next sections, we will address the modeling challenges concerning particle force models, interphase coupling, effect of the nozzle walls, and maintaining high-order accuracy through the simulation domain.

1.1 Particle force models

Proper choice and modeling of the forces acting on solid particles are primarily important. Bhattacharya et al. [9] and Kudryavtsev et al. [10] emphasized the relative importance of drag force against others for a nozzle gas flow laden with micron-sized solid particles. Drag force that accounts for inertial, compressibility, and rarefaction effects should be retained. Empirical correlations explicitly containing all these effects were applied in Molleson and Stasenko [11] and Kudryavtsev et al. [10]. However, such correlations contain several uncertain model coefficients. This impedes their convenient and creditable applications. Alternatively, another empirical correlation for drag coefficient improved by Parmar et al. [12], which was developed according to comprehensive data [13], will be utilized in the current modeling in consideration of the estimated Knudsen numbers of $O(10^{-2})$ or smaller in this study. The consideration of collision force is due to two main reasons. First, we would like to access its relative importance compared with the drag force. Second, we plan to make the current model applicable to gas-particle flows with particle mass loading much greater than the maximum in this study. Stewart et al. [14] directly computed collision forces by using a soft-sphere model. Such a model also can be adopted in the current gas-particle system, but is computationally expensive. Alternatively, Harris and Crighton's particle-stress type of collision force model [15] will be employed due to its wide-spread success in other simulations and low computation requirement suited for design.

1.2 Interphase coupling

For situations with very low particle mass loadings, the neglect of reverse influence of the particle phase to the gas phase (i.e., so-called one-way coupling) should be reasonable at some extent. However, this usually does not hold in the present cases. On the contrary, the coupling of the particle phase can significantly affect the two-phase flow field, and thus, it is not ignorable. Consequently, a four-way interphase coupling that accounts for interactions of the gas-particle phases and collisions of the particles simultaneously will be adopted in this modeling. For the large number of particles present in a real system, tracking each individual particle velocity and thermal history quickly becomes prohibitive. Fortunately, we can resort to a point particle approach (PPA) and a concept of computational (or representative) particle used in Ling et al. [16] among others. The former avoids resolving the flow around each individual particle by applying empirical correlations. The latter avoids tracking each physical particle as a point particle. In such a method, each computational particle represents a certain number of physical particles. One only needs to track this computational particle as a point particle in a Lagrangian way when performing the computations of the particulate phase. On the other hand, when solving the gas-phase equations, it is required to take into account the coupling of the real number of physical particles represented by this computational particle. As a result, the computations for tracking the particle velocity and

thermal histories can be greatly reduced, and meanwhile, the real interphase coupling between the particulate and gaseous phases also can be validly modeled.

1.3 Effect of nozzle walls

In the process of a particle-laden gas flow expanding through a de Laval nozzle, friction and heat exchange occur between the gas flow and nozzle walls. The throat Reynolds number, defined by the distance from the nozzle inlet to the throat, is 2.5×10^6 or larger in the present simulations. This value exceeds the critical Reynolds number for transition, resulting in a turbulent boundary layer for most of the divergent section. Luo et al. [17] modeled and numerically simulated quasi-one-dimensional, steady, supersonic gas flows with particles in a de Laval nozzle with a long and conical expansion section. In that work, they took account of the wall friction and heat transfer effects on the gas phase by applying a turbulent boundary layer model on a flat plate. In comparison, each of the currently adopted nozzles has a wedge-like divergent section with flat-plate walls. This flat-plate turbulent boundary layer model is more applicable to the present modeling. For the presently analyzed nozzles with rectangular cross sections, the interference of boundary layers at the corners of the internal walls is inevitable. As a result, the local velocity and temperature variations within the boundary layers will be changed slightly. The flat-plate turbulent boundary layer model in Luo et al. [17] should be corrected for the present modeling in view of the difference of geometries between the nozzle internal walls and flat plates.

1.4 Uniformly high-order accuracy

A uniformly high-order accurate numerical method, meaning that this method satisfies the required high-order accuracy everywhere, is extremely important for the present simulation of particle-loaded compressible gas flows [18]. However, it is hard to preserve the high-order accuracy uniformly in the whole solution domain. When one employs a high-order (e.g., third-order) scheme for the discretization of convective terms, the uniformly high-order accuracy will be destroyed by applying a lower-order scheme for the approximation of diffusive terms or for the boundary treatment [19,20]. In order to avoid these problems, a WENO scheme [21], which is fifth-order accurate in smooth regions and meanwhile third-order accurate at discontinuities, will be selected to discretize the convective flux vector of the gas phase. The discretization will be based on a characteristic splitting for the gas-phase flux vector with a modified Steger–Warming splitting method [18]. Furthermore, third-order upwind schemes will be constructed for the approximation of first derivative terms of the remaining quantities. Additionally, a third-order

polynomial interpolation of gaseous properties at particle positions also will be applied.

1.5 Objectives

In the present study, the main objectives are set as the following four aspects (1): to construct a simple and effective quasi-one-dimensional gas-particle flow model in the de Laval nozzle (2); to create a set of uniformly high-order accurate, stable, and efficient numerical methods (3); to calibrate and then validate the numerical prediction model (4); and to perform the parametric study.

2 Modeling of gas-particle two-phase flow

2.1 Equations for gas phase

The gas-phase flow equations are numerically solved with a time-dependent method, and thus, a steady-state asymptotic solution is attained by performing the integration until the flow field fails to change with time. Specifically, we express the gas-phase flow by inviscid, compressible, unsteady, quasi-one-dimensional nozzle flow equations and meanwhile incorporate the molecular and turbulent viscous effects with source terms that reflect the influence of the particulate phase and nozzle walls. Using Cartesian coordinates, the conservation equations in vector form for the gas phase are given as follows:

$$\frac{\partial \mathbf{U}}{\partial t} + \frac{\partial \mathbf{F}}{\partial x} = \mathbf{S} \tag{1}$$

$$\mathbf{U} = \left[\rho_g \alpha, \rho_g \alpha v_g, \rho_g \alpha e^* \right]^T \tag{2}$$

$$\mathbf{F} = \left[\rho_g \alpha v_g, \rho_g \alpha v_g^2 + p, (\rho_g \alpha e^* + p) v_g \right]^T \tag{3}$$

$$\mathbf{S} = [s_1, s_2, s_3]^T \tag{4}$$

$$\begin{cases} s_1 = -\rho_g \alpha v_g \frac{1}{A} \frac{\partial A}{\partial x} \\ s_2 = -\rho_g \alpha v_g^2 \frac{1}{A} \frac{\partial A}{\partial x} + f_{wf} - \frac{1}{V_{cell}} \sum N_{cp} f_i^{gp} \\ s_3 = -\rho_g \alpha e^* v_g \frac{1}{A} \frac{\partial A}{\partial x} - p v_g \frac{1}{A} \frac{\partial A}{\partial x} + \\ \quad Q_W + G_W - \frac{1}{V_{cell}} \sum N_{cp} \left(G_i^{gp} + Q_i^{gp} \right) \end{cases} \tag{5}$$

where $\mathbf{U}$ is the primitive vector of solution, $\mathbf{F}$ the flux vector, $\mathbf{S}$ the source vector, ρ_g the material density of the gas, α the volume fraction of the gas phase, v_g the gas velocity, p the static pressure, and e^* the specific total energy, namely the sum of the specific internal energy e and kinetic energy $v_g^2/2$. Besides, x is measured along the nozzle axis, t the lapsed time, A the cross-sectional area, f_{wf} the wall friction per unit cell volume, f^{gp} the gas flow force on a particle, V_{cell} the grid cell volume, subscript "i" the number of a computational particle, Q_w the heat transfer rate from the walls per unit cell volume, G_w the frictional rate of work by the walls,

G^{gp} the rate of work on a particle caused by the gas flow force, and Q^{gp} the rate of heat transfer to a particle from the gas. It should be emphasized that N_{cp} is the real number of physical particles represented by one computational particle, and thus, only $1/N_{\mathrm{cp}}$ of the total number of physical particles need to be tracked during the computation for the particulate phase, while the coupling of all the physical particles is taken into account during the gaseous phase computation. The final two terms G^{pg} and Q^{pg} in s_3 of (5) represent the cell-volume averaged rate of work and heat transfer rate from the particles to the gaseous medium, respectively.

The wall friction f_{wf} is expressed as

$$f_{\mathrm{wf}} = -2C_f \rho_g v_g^2 / D \tag{6}$$

where D is the local equivalent diameter of the wetted perimeter. The wall friction coefficient C_f and Stanton number C_h can be given by

$$C_f = C_1 \left(\frac{h_{\mathrm{g}}}{h_{\mathrm{g0}}} \right)^{C_2} \left(\frac{h_{\mathrm{w}}}{h_{\mathrm{g0}} Re_x} \right)^{C_3} \tag{7}$$

$$C_h = 0.53 C_f \tag{8}$$

where $C_1 = 0.15\zeta$, $C_2 = 0.4$, and $C_3 = 0.2$. The currently introduced boundary layer correction factor ζ, which is close to unity, can be calibrated with experimental data of nozzle flows. Besides, h_{g} and h_{g0} are the static and stagnation specific enthalpies of the gas, respectively. The wall enthalpy h_{w} is defined as $c_{\mathrm{pg}} T_{\mathrm{w}}$ at a given wall temperature T_{w}. The specific heat of the gas at constant pressure c_{pg} can be considered as a function of temperature. Reynolds number at x position is defined by

$$Re_x = \rho_g v_g x / \mu \tag{9}$$

where the dynamic viscosity of the gas μ is calculated with Sutherland's law. The wall heat transfer rate Q_{w} and frictional rate of work G_{w} are, respectively, expressed as

$$Q_{\mathrm{W}} = -4C_h \left(h_{\mathrm{g0}} - h_{\mathrm{W}} \right) / D \tag{10}$$

$$G_{\mathrm{W}} = f_{\mathrm{wf}} v_g. \tag{11}$$

Finally, the ideal gas equation of state is necessary for the enclosure of equations.

2.2 Equations for particle phase

The particles are regarded as a discrete phase, and the representative computational particles are tracked with a Lagrangian method. The equations of motion, position, and energy are given as follows:

$$m^{\mathrm{p}} \frac{\mathrm{d}v_{\mathrm{p}}}{\mathrm{d}t} = f_i^{\mathrm{gp}} + f_i^{\mathrm{pp}} \tag{12}$$

$$\frac{\mathrm{d}x_{\mathrm{p}}}{\mathrm{d}t} = v_{\mathrm{p}} \tag{13}$$

$$\frac{1}{6} \pi \mathrm{d}_{\mathrm{p}}^3 \rho_{\mathrm{p}} c_{\mathrm{p}} \frac{\mathrm{d}T_{\mathrm{p}}}{\mathrm{d}t} = Q_i^{\mathrm{gp}} \tag{14}$$

where m^{p} is the mass of a single particle, f^{pp} is the collision force between particles, v_{p}, x_{p}, ρ_{p}, d_{p}, T_{p}, and c_{p} are the particle velocity, position, density, diameter, temperature, and specific heat, and π is the circumference ratio. The drag force of the gas flow on ith particle is determined by

$$f_i^{\mathrm{gp}} = \frac{\pi}{8} d_{\mathrm{p}}^2 \rho_g C_{\mathrm{D}} \left(v_g - v_{\mathrm{p}} \right) \left| v_g - v_{\mathrm{p}} \right|. \tag{15}$$

The drag coefficient C_{D} utilizes Parmar et al.'s correlation which had a level of error below 2.5% [12]. For present purposes, the definitions of particle Reynolds number $\mathrm{Re_p}$, Mach number M_{p}, and Knudsen number $\mathrm{Kn_p}$ are given as

$$\mathrm{Re_p} = \rho_g \left| v_g - v_{\mathrm{p}} \right| d_{\mathrm{p}} / \mu \tag{16}$$

$$M_{\mathrm{p}} = \left| v_g - v_{\mathrm{p}} \right| / a \tag{17}$$

$$\mathrm{Kn_p} = 1.256 \sqrt{\gamma} M_{\mathrm{p}} / \mathrm{Re_p} \tag{18}$$

where a is the local sound speed and the ratio of specific heats of the gas γ can be treated as a function of the gas temperature T_{g}. In the present analysis, a cubic spline interpolation is employed to calculate the gas enthalpy, specific heats at constant pressure and at constant volume, and the ratio of specific heats for air by applying Jones and Dugan's thermodynamic property data [22]. On the other hand, Newton-downhill method is used to find solutions of the gas temperature. Note that all the properties of the gas phase in (16)–(18) should take the values of the gas phase at the position where the particle resides. The calculation of collision forces f^{pp} is based on Harris and Crighton's classic model [15]. A simple derivation gives

$$f_i^{\mathrm{pp}} = -\frac{V_{\mathrm{p}} P_{\mathrm{s}} \left[\beta \left(\varphi_i \right)^{\beta-2} \left(\varphi_c - \varphi_i \right) + \left(\varphi_i \right)^{\beta-1} \right]}{\left(\varphi_c - \varphi_i \right)^2} \frac{\partial \varphi_i}{\partial x} \tag{19}$$

where V_{p} is the volume of a single particle and φ_i the local particle volume fraction in the grid cell where the ith particle resides. The particle volume fraction at close packing is specified as $\varphi_c \approx 0.6$ for mono-sized spherical particles. The model constants $P_{\mathrm{s}} = 2 \times 10^5 \mathrm{Pa}$ and $\beta = 3$ were used as suggested by Snider et al. [23].

The rate of work G^{gp} in (5) equals the product of the gas flow force f^{gp} and the particle velocity v_{p}. The gas heat transfer to a particle happens mainly convectively in the present study, and thus, the heat transfer rate can be computed by

$$Q_i^{\mathrm{gp}} = \mathrm{Nu} \pi \mu c_{\mathrm{pg}} d_{\mathrm{p}} \left(T_{\mathrm{g}} - T_{\mathrm{p}} \right) / \mathrm{Pr} \tag{20}$$

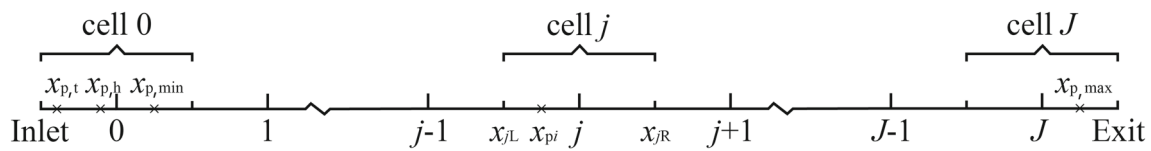$$\mathrm{Pr} = 4\gamma / \left(9\gamma - 5 \right). \tag{21}$$

Fig. 2 Schematic of the distribution of particle positions

Nusselt number Nu is calculated according to Drake's [24] empirical correlation which had a level of error within $\pm 1\%$.

2.3 Injection and statistical strategies of particles

We lay out $J+1$ grid nodes with a uniform spacing Δx along the quasi-one-dimensional nozzle and define any region with a length of Δx and a center being situated at node j as cell j, whose left and right boundary locations are denoted by x_{jL} and x_{jR}, respectively. The maximum and minimum positions of computational particles are denoted by $x_{p,max}$ and $x_{p,min}$, as shown in Fig. 2. At each time step, a batch of particles is instantaneously injected into the nozzle from the inlet at the same time by designating the location, velocity, and temperature for each particle. The head and tail positions of this batch of particles are represented by $x_{p,h}$ and $x_{p,t}$, respectively.

Given a nozzle-inlet particle mass loading ψ, which is defined by the ratio of particle mass to gas mass, the particle mass flow rate q_{mp} can be calculated by

$$q_{mp} = \frac{\rho_p v_p A}{1 + \left[\rho_p / (\psi \rho_g)\right]}. \tag{22}$$

The relation between particle mass loading ψ and particle volume fraction φ can be expressed as

$$\psi = \frac{\varphi \rho_p}{(1 - \varphi) \rho_g}. \tag{23}$$

Given a computational particle number being injected every time step N_{inj}, the real number represented by one computational particle is

$$N_{cp} = q_{mp} \Delta t / \left(\rho_p V_p N_{inj}\right). \tag{24}$$

The injected computational particle number at initial time is determined by

$$N_{inj}^{(0)} = \text{Int}\left(q_{mp} \Delta t / \left(N_{cp} \rho_p V_p\right)\right) \tag{25}$$

where "Int()" denotes an integer function that takes the integer portion of the value in the parentheses. The error because of integer calculations accumulates time after time. As a result, it will exceed unity at an injection. A correction required for the injected computational particle number is

expressed as

$$N_{inj}^{(n)} = \text{Int}\left\{\frac{(n+1) q_{mp} \Delta t}{N_{cp} \rho_p V_p} - \left(\sum_{l=1}^{n-1} N_{inj}^{(l)}\right)\right\} \tag{26}$$

where the superscripts "(l)" and "(n)" represent time steps. For a newly injected batch of particles, the positions are assigned as

$$x_{pi} = i v_p \Delta t / N_{inj}^{(n)} \left(i = 2, \ldots, N_{inj}^{(n)}\right). \tag{27}$$

All these particles take the same velocity and temperature values as those at the nozzle inlet. All the remaining particles are reordered. For any cell j, the total number of particles N_{JI} and the numbers of the particles, whose coupling needs to be accumulated in (5), can be determined by a loop for the new particle numbers. Thus, the local particle volume fraction is computed by

$$\varphi_i = N_{JI} V_p / V_{cell}. \tag{28}$$

It should be supplemented that the sum of local gas and particle volume fractions is unity.

3 Conditional parameters and model validation

3.1 Geometrical and computational parameters

The relevant geometric parameters for the de Laval nozzles used in this study are presented in Fig. 3. There are two types of geometry in this study. Type I models applied in Meyer et al.'s [25] experiments are only used for the validation of the current numerical model. Type II that was used for supersonic gas–solid separation [2] is employed to conduct the following parametric study. Type II can be regarded as a special case of Type I without the planar convergent section. The detailed geometric parameters are listed in Table 1.

Table 2 shows the changeable computational parameters used for the validating calculations. Other parameters are fixed, such as the nitrogen gas constant $R = 296.7 \, \text{J kg}^{-1} \, \text{K}^{-1}$, ratio of specific heats $\gamma = 1.4$, and particle diameter $d_p = 30 \, \mu\text{m}$. Table 3 presents the changeable parameters for the parametric study. Other fixed parameters
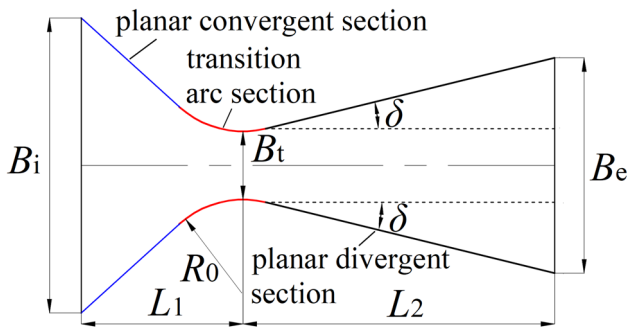
Fig. 3 Schematic of longitudinal profile of the nozzles

include the gas constant of air $R = 287.05$ J kg^{-1} K^{-1}, particle density $\rho_p = 1500$ kg m^{-3}, particle specific heat $c_p = 1437.2$ J kg^{-1} K^{-1}, and expansion angle $\delta = 3.44°$.

3.2 Boundary conditions

The inlet stagnation temperature T_0, stagnation pressure p_0, particle mass loading ψ, and uniform wall temperature T_w are given. In the computations for validation, we set $T_0 = 293$ K, $p_0 = 600$ kPa, $\psi = 0.05$–0.20, and $T_w = 293$ K. In the cases for parametric study, $T_0 = 300$ K, $p_0 = 529$ kPa, $\psi = 1.161$ (or $\varphi = 10^{-3}$), and $T_w = 300$ K. At the nozzle inlet, $T_p = T_g$, and $v_p = v_g$. They are not given but automatically updated from an initial flow field. We adopt a compatibility condition on the c^- characteristic [26] under the assumption that the gas medium and particles are in equilibrium with each other in velocity and temperature. The inlet two-phase velocity is restrained by

$$
\begin{aligned}
\left[(1+\psi)\, v_g \rho_g \alpha + \rho_g \alpha a\right] & \frac{\partial v_g}{\partial t} \\
= (v_g - a)\frac{\partial p}{\partial x} - \rho_g \alpha a(v_g - a) & \frac{\partial v_g}{\partial x} \\
+ a^2 \rho_g \alpha v_g \frac{1}{A}\frac{\partial A}{\partial x} - aK_2 - (\gamma - 1) & K_3
\end{aligned}
\tag{29}
$$

where the parameters were set as $K_2 = f_{wf}$ and $K_3 = Q_w + G_w$, respectively.

For the supersonic gas flows, all the gas-phase parameters at the exit boundary can be extrapolated from the internal nodes and thus need not be given.

3.3 Calibration for model correction factor ζ

Note that the numerical methodology used in this study may be found in Appendix. In order to determine an optimal boundary layer correction factor ζ in (7), we perform the computations of nozzle air flow under Gao et al.'s experimental condition [2]. The uncertainty of their experimental data was $\pm 0.5\%$ according to the accuracy of the adopted instruments. A relative error function of pressure is defined as

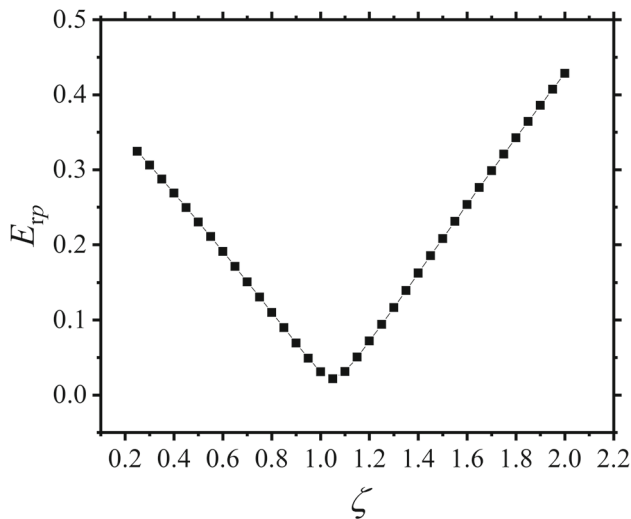**Table 1** Geometric parameters for the two types of nozzles

Type number	Convergent length L_1 (mm)	Divergent length L_2 (mm)	Inlet height B_i (mm)	Throat height B_t (mm)	Transition arc radius R_0 (mm)	Exit height B_e (mm)	Uniform width B (mm)	Expansion angle δ (°)
I	30	120	17.72	1.02	10	3.8	3.07	Definite
II	40	400	92	12	40	Variable	12	Variable

Table 2 Computational parameters for validation

Particle species	Inlet particle mass loading ψ	Particle specific heat c_p (J kg^{-1} K^{-1})	Particle density ρ_p (kg m^{-3})
Titanium	0.05–0.20	520	4506
Stellite-21	0.05–0.20	417	8300

Table 3 Computational parameters for parametric study

Particle diameter d_p (μm)	Inlet particle mass loading ψ	Inlet stagnation pressure p_0 (kPa)	Inlet stagnation temperature T_0 (K)	Nozzle expansion angle δ (°)
5	0.111	529	300	2.50
10	0.429	700	400	3.00
30	1.000	1000	500	3.44
50	2.333	1200	600	4.00
100				

Fig. 4 Variation of the relative error function E_{rp} with the boundary layer correction factor ζ

$$E_{rp} = \sqrt{\frac{1}{n} \sum_{i=1}^{n} [(p_{ci} - p_{mi})/p_{mi}]^2} \qquad (30)$$

where p_c and p_m are the computational and measured pressures, respectively. The measured data $p_m = 48.714, 29.963, 29.098$, and 28.284 kPa at positions $x = 180, 300, 310$, and 320 mm, respectively. In a large range of ζ changing from 0.25 to 2.0, the minimum value of E_{rp} is achieved at $\zeta = 1.05$ (see Fig. 4). As explained above, this slight deviation of the correction factor from unity is caused by the effect of boundary layer interference at internal corners of the nozzle. This value of ζ is adopted for all the subsequent computations.

3.4 Verification for grid independence

In order to verify the grid independence, we perform the computations for a gas-particle two-phase flow in a Type II nozzle by using three different spatial steps, i.e., $\Delta x = 0.5, 0.8$, and 1.0 mm, respectively. Aside from the fixed parameters for air mentioned above, other parameters are specified as the particle diameter $d_p = 30$ μm and time step $\Delta t = 5 \times 10^{-7}$ s. It can be seen from Fig. 5 that the difference of the curves for flow field parameters (partially presented) is indistinguishable, and thus, we believe that the grid independence has been held when $\Delta x = 1.0$ mm, and therefore, this spatial step is used for the below calculations.

3.5 Validation for the numerical model

Figure 6a shows the present computational particle velocities in the whole of the Type I nozzle at inlet particle mass loadings $\psi = 0.05$ and 0.20 for stellite-21 particles (denoted by CMP), and Meyer et al.'s measured data [25] (denoted by EXP). One can observe that the uncertainty of the measurement data can be very large. For example, the uncertainty exceeds 50% at the nozzle inlet, which then falls below 6.58% at the exit. Furthermore, we can find that the calculated particle velocities completely fall into the corresponding uncertainty ranges of measurements.

Figure 6b presents a comparison of our present computational particle velocities at the exit for both titanium and stellite-21 particles under different particle mass loadings with Meyer et al.'s experimental results [25]. It can be found that both the experimental and our computational data of particle velocities at the exit tend to decrease with increasing
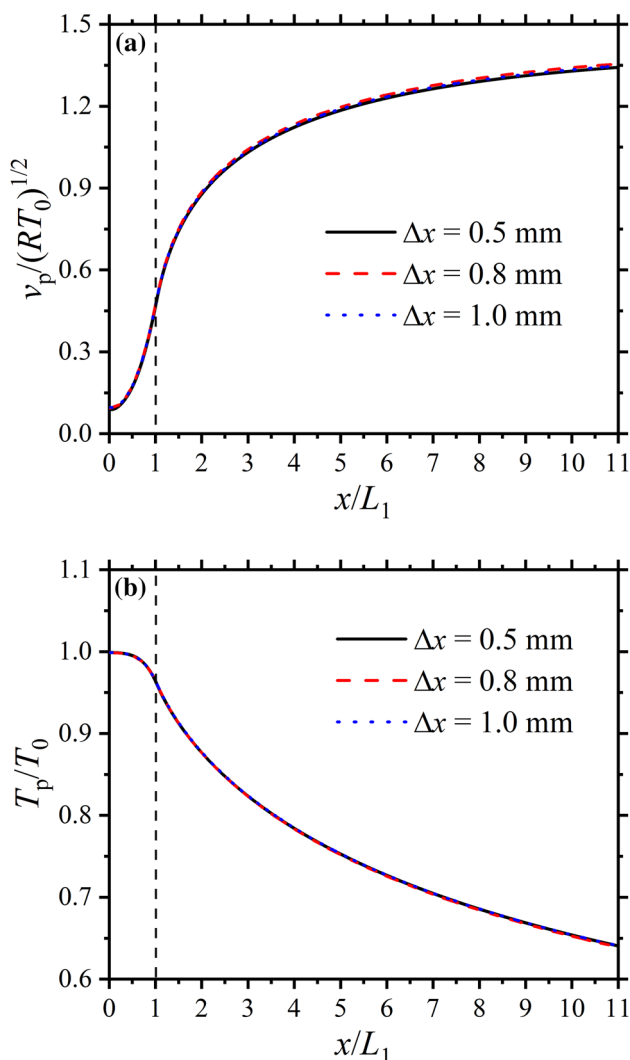
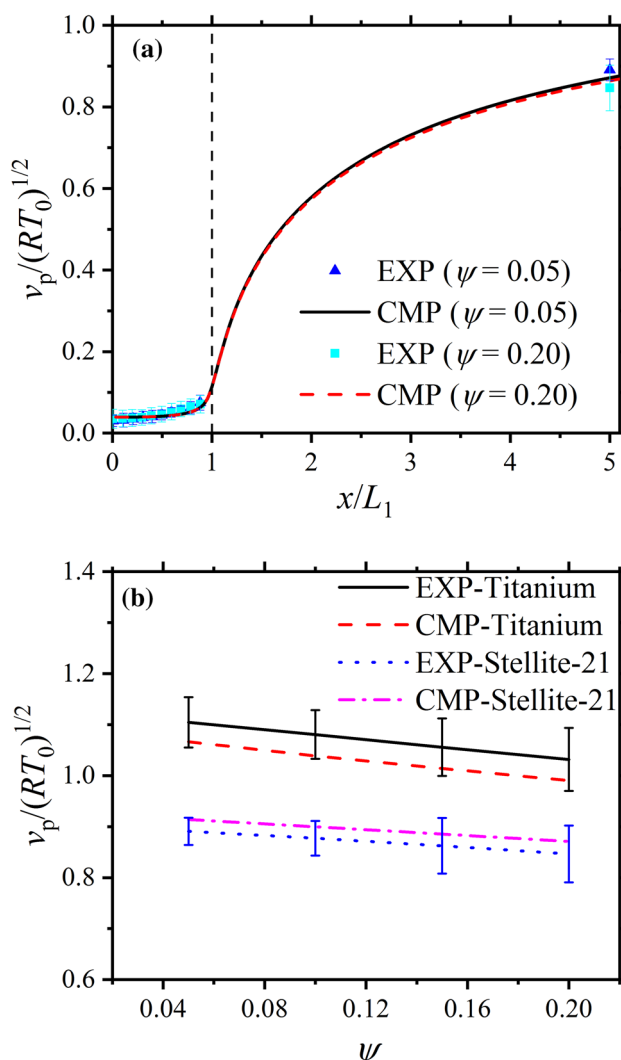**Fig. 5** Comparison of computations at different spatial steps for a gas-particle two-phase flow

Fig. 6 Computational particle velocities **a** in the whole nozzle for stellite-21 particles and **b** at the exit for both titanium and stellite-21 particles versus Meyer et al.'s experimental data [25]

particle mass loading. Detailed data comparisons show the maximum relative errors of 2.88% and 4.20% for titanium and stellite-21 particles, respectively, at different particle mass loadings of $\psi = 0.05$–0.20.

The possible sources of departure of the simulation from the experiment contain at least the following two aspects. One is that the experiment involved a polydisperse gas-particle system, but we treated the particles as monodisperse, using the average diameter provided by the experimentalists. The other is that their particle tracking velocimetry measurement method led to some level of errors, as claimed by the experimentalists. However, all the simulation errors are within the experimental uncertainty. The comparisons described as above demonstrate the validity and accuracy of the present numerical model.

4 Results and analyses

It should be noted that all the results present in this section are from Type II geometry of the de Laval nozzles.

4.1 Effect of particle size

Figure 7a–d presents the plots of the gas flow force f^{gp}, unit-particle-mass gas flow force a^{gp}/g (non-dimensionalized by $g = 9.8$ m s^{-2}), collision force f^{pp} on each particle, and particle volume fraction φ, respectively. It is can be seen that both the f^{gp} and a^{gp}/g increase from the near-zero nozzle inlet values to the maximum values at positions close to the nozzle throat and then decrease gradually to the exit values. Furthermore, a larger particle size always leads to a greater gas flow force. A smaller particle has a greater unit-particle-

mass gas flow force (extremely close to the acceleration) in the convergent section and a portion of the divergent section, but an inversion will happen in the remaining portion of the divergent section only if its length is long enough. We can see from Fig. 7b that the a^{gp}/g for a 5-μm particle drops down from the largest at the throat to the smallest at the exit. According to the definition of velocity relaxation time $\tau_v = \rho_P d^2_P/18\mu$, we know that a smaller particle spends a shorter time on the equalization of the gas-particle velocity difference. Therefore, once the interphase velocity difference is significantly decreased, the acceleration of this smaller particle will decrease faster.

The variation of the collision force appears to be more complex. One can see from Fig. 7c that the collision force increases a little from an inlet negative value first, then falls down to a valley with negative values, next quickly climbs to a positive peak near the throat, thereafter gradually declines, and finally tends to a zero value. Note that the negative sign of the collision force means that its direction is pointing toward the inlet of the nozzle and is not related to the magnitude. The increase in the particle size leads to the conspicuous increase in the collision force.

Figure 7d indicates that particle volume fraction increases from an inlet value to a peak in the convergent section and subsequently falls down gradually. Furthermore, the local particle volume fraction including the peak value increases with increasing particle size, although all the inlet φ values are the same in these cases. This implies that large particles have a further tendency to stagnate in the nozzle, especially in the convergent section due to the relatively large inertias. Close inspection reveals that each extreme point of φ curve corresponds to a zero of collision-force curve, and meanwhile, each inflection point of φ curve that is close to the throat corresponds to a maximum value of collision force. The first half of this finding seems counter-intuitive, but is reasonable indeed. We should realize that in the present quasi-one-dimensional analysis, the collision force of a particle is the axial resultant force due to collisions of particles in the neighboring two grid cells. The collision force from each side should be the maximum at the extreme point of φ, but a dynamic balance of the two-side collision forces should also be achieved there.

Additionally, we can see from Fig. 7a–c that the collision forces are much smaller than the corresponding gas flow forces. For example, the analyzed maximum values of the collision force and the gas flow force have orders of magnitude of $O(10^{-10}\,\text{N})$ and $O(10^{-4}\,\text{N})$, respectively. This means collision forces in the similar applications related to dilute gas-particle flows are negligible.

Figure 8a, b presents the plots of the particle velocity $v_p/(RT_0)^{1/2}$ and gas Mach number M_g for different particle sizes, respectively. We can see that both the particle velocity and gas Mach number increase monotonically with axial
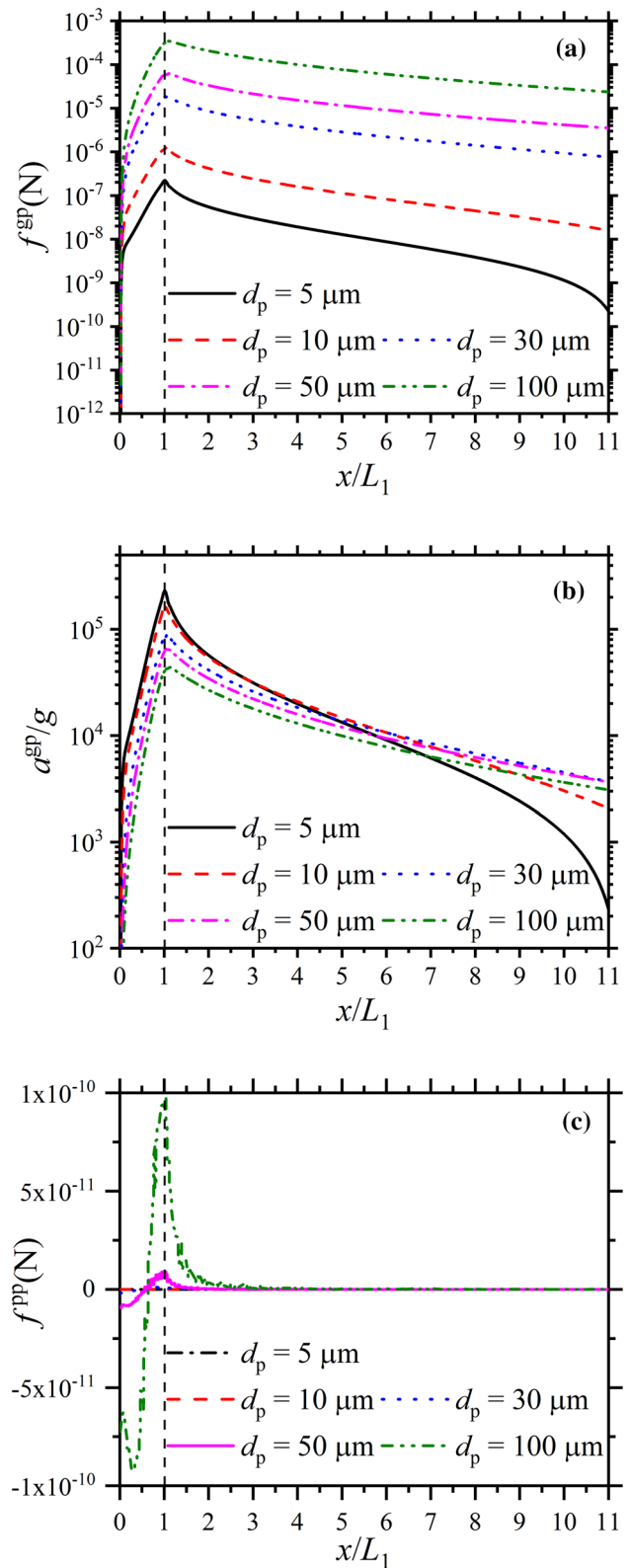
Fig. 7 Plots of **a** f^{gp}; **b** a^{gp}; **c** f^{pp}; and **d** φ for $\psi = 1.161$ at different particle sizes

Fig. 7 continued

Fig. 8 Plots of **a** $v_p/(RT_0)^{1/2}$ and **b** M_g for different particle sizes
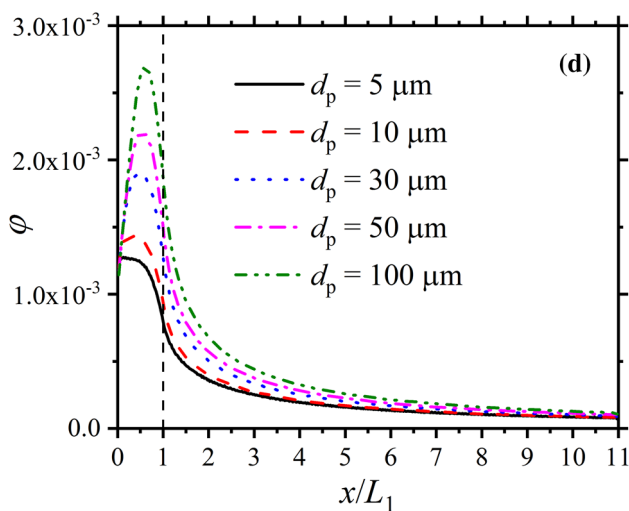
position. The increase in the particle size decreases the particle velocity while increasing the gas Mach number. From the preceding analysis, we know that a large particle attains a lesser acceleration at first and thus equalizes the gas-particle velocity difference more slowly than a small one. As a result, the large particle moves more slowly than the small one at any location within the nozzle. That means a unit mass of large particles obtains less kinetic energy from the gaseous medium than that of small particles. Therefore, the gas velocity should be decreased less by the large particles than by the small particles. On the other hand, the large particles have smaller heat transfer area per unit mass than the small particles. Therefore, the former lose less internal energy to the gas medium and retain higher temperatures than the latter. Consequently, the gas temperature and thus the local sound speed corresponding to the large particles are lower than those corresponding to the small particles. This explains why a large particle size leads to a large gas Mach number.

The gaseous medium expands dramatically and tends to the sound speed just upstream of the throat position. However, the solid particles cannot catch up with the gas flow due to their larger inertias, although they are also accelerated to some extent in the convergent section. It can been seen from Fig. 9a–b that both the particle Reynolds and Mach numbers increase from the small inlet values to the near-throat maximum values and subsequently decrease gradually. This explains the appearance of the maximum gas flow force at the near-throat location and its whole variation with axial position. Furthermore, one can find that the larger the particle size, the greater the particle Reynolds and Mach numbers. For the minimum-sized particles, the velocity difference between the two phases nearly disappears at the nozzle exit. By contrast, the maximum-sized particles retain relatively high exit velocity difference. It should be noted that the particle Mach
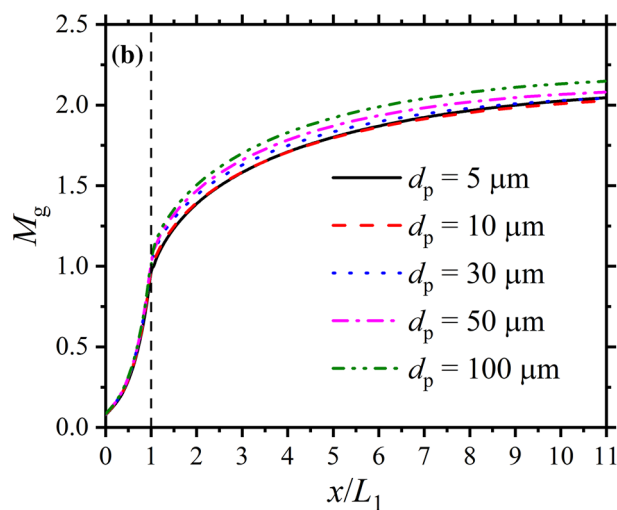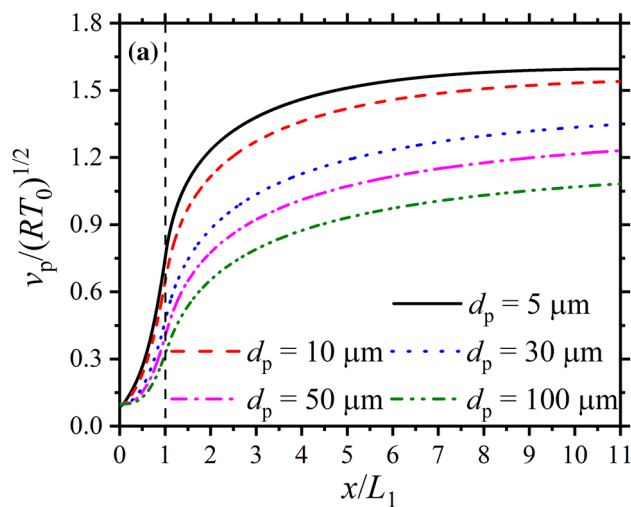
numbers for the two larger sizes pass the critical value of around 0.6 where shocklets begin to form on the particles.

Figure 9c presents the local particle Knudsen numbers Kn_p along the nozzle axis for the investigated particles. Note that the limitation of the particle Knudsen number in the adopted Parmar et al.'s drag correlation [12], which implicitly contained the rarefaction effect, is $Kn_p < 0.01$. We can see from Fig. 9c that all the calculated Kn_p values for the particles with diameters from 10 to 100 µm are below 0.01, and only the one for the smallest 5-µm particles slightly exceeds the limitation of the continuum model near the nozzle exit. The obtained particle Knudsen numbers support the validity of the drag model for this study. An additional correction for the rarefaction effects is not necessary.

Figure 9d shows the local Reynolds numbers Re_x along the nozzle axis for different particle sizes. It can be seen that all the Reynolds numbers in the divergent section fall in a range of about 2.5×10^6–1.2×10^7. The critical Reynolds
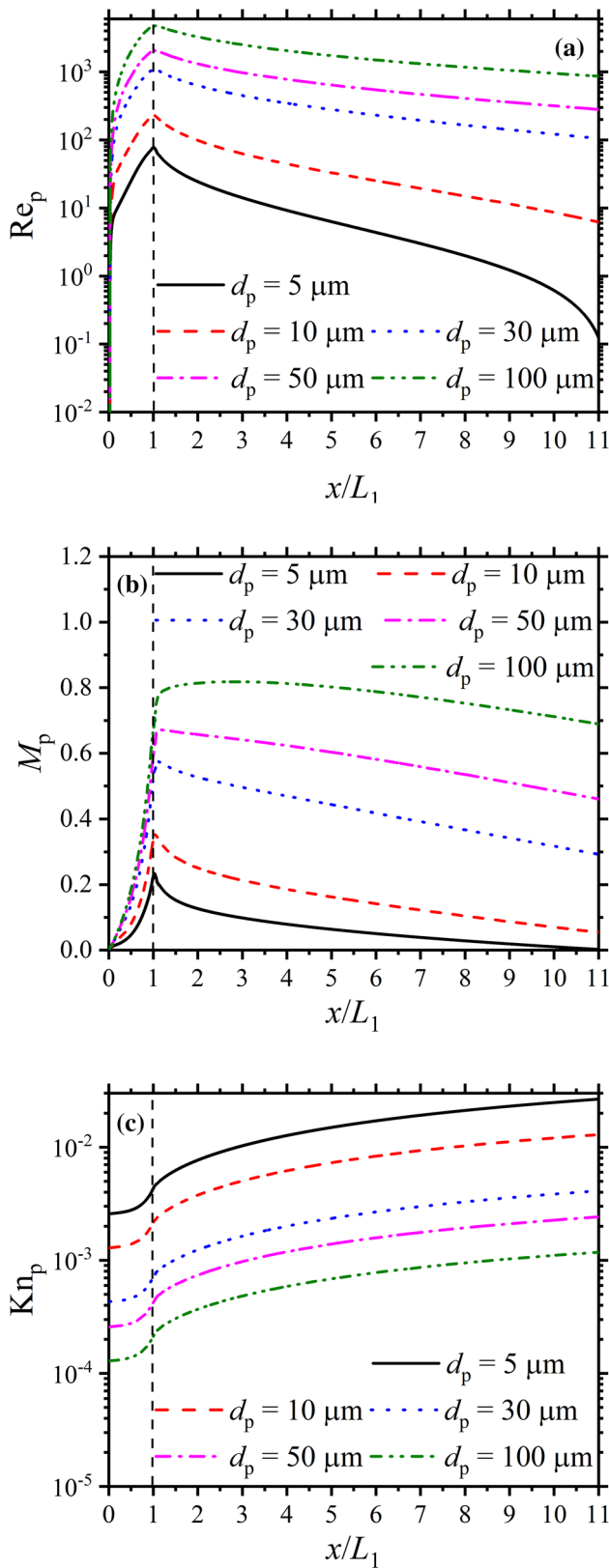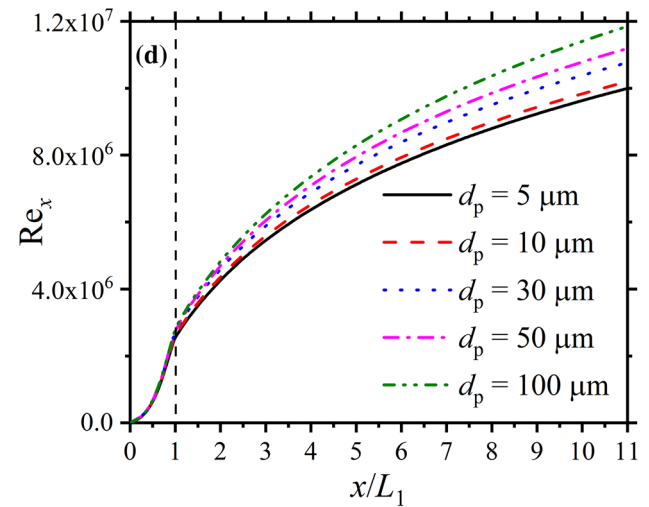
Fig. 9   continued

number for transition to turbulence for a flat-plate flow is below 4.0×10^6. Moreover, a finite turbulence intensity of the incoming flow is expected in a real-world application, significantly decreasing the critical Reynolds number. Consequently, the boundary layer is turbulent over the length of the divergent section and indicates the necessity for applying a turbulent boundary layer model such as the presently corrected version based on that in Luo et al. [17].

4.2 Effect of particle mass loading

Figure 10a–c presents the plots of the particle velocity $v_p/(RT_0)^{1/2}$, gas Mach number M_g, and particle volume fraction φ at different inlet particle mass loadings, respectively. We can see that the increase in the particle mass loading limits the rises of the particle velocity and gas Mach number and also increases the particle volume fraction. The increase in the particle mass loading firstly means that the particles carry more total internal energy initially. Its most direct result is that the particle temperatures decline more slowly. Given a local gas temperature in a grid cell, more heat is transferred from the particles to the gaseous medium in this cell because of a higher temperature difference between them. As a result, the speed of decline in the gas temperature caused by the volume expansion becomes slower. Additionally, the particles occupy more space in the current situations and thus make the local particle volume fraction greater. The expansion of the gaseous medium is naturally suppressed in the nozzle. Therefore, the speed of increase in the gas velocity becomes slower. The relatively small gas velocity and high gas temperature cause the relatively small gas Mach number. Given a local velocity of a particle, the decrease in the velocity difference between the gas and this particle certainly leads to
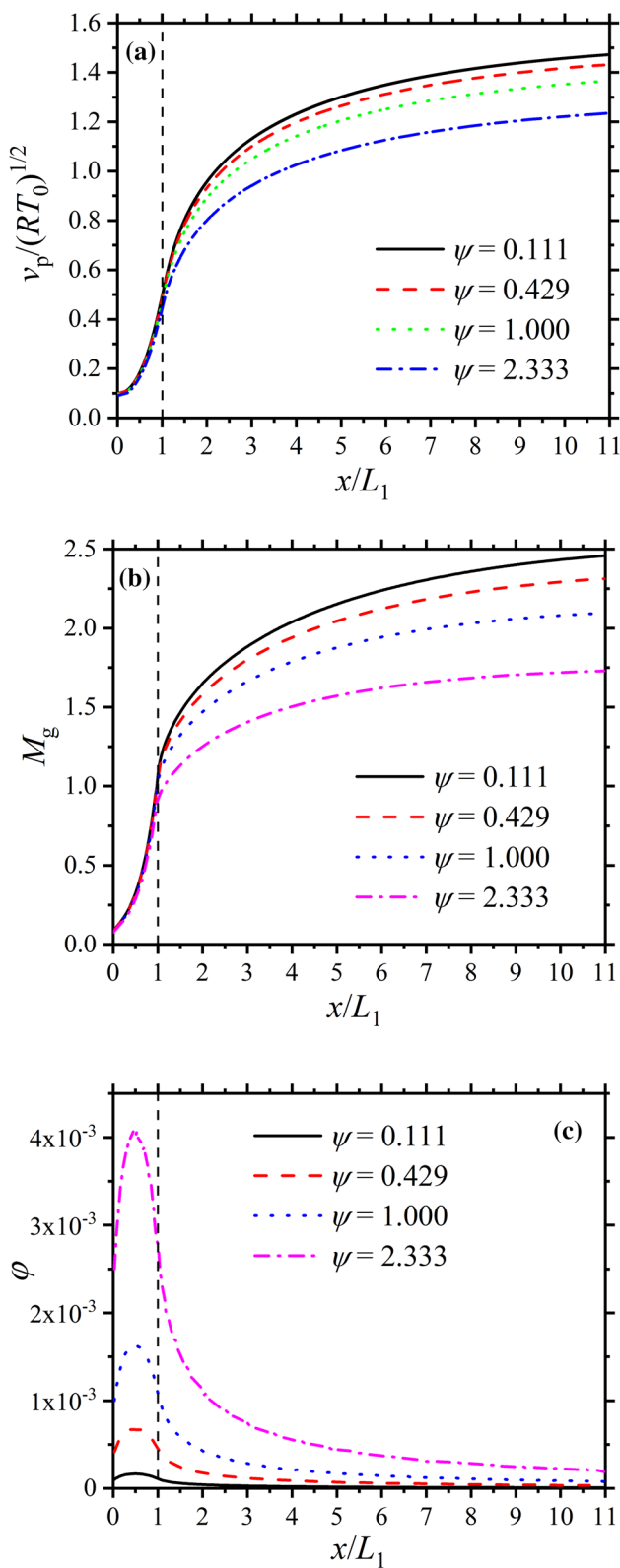
Fig. 9   Plots of **a** Re_p; **b** M_p; **c** Kn_p; and **d** Re_x for different particle sizes

Coupled modeling and numerical simulation of gas flows laden with solid particles...

225

Fig. 10 Plots of **a** $v_p/(RT_0)^{1/2}$; **b** M_g; and **c** φ at different inlet particle mass loadings

the decrease in the acceleration of this particle and thus the decrease in the succeeding particle velocity.

4.3 Effect of inlet stagnation pressure

Figure 11a–c presents the plots of the particle velocity $v_p/(RT_0)^{1/2}$, gas Mach number M_g, and particle volume fraction φ at different inlet stagnation pressures, respectively. It can be observed that the increase in the inlet stagnation pressure increases the particle velocity and gas Mach number while decreasing the particle volume fraction. As the inlet stagnation pressure rises significantly, the static pressure at any axial position naturally rises, but the increase in the exit static pressure is quite limited. The increased differential pressure force pointing to the nozzle exit is able to suppress the development of the boundary layers and also to overcome the wall friction more effectively. Consequently, the gas medium expands more smoothly and thus obtains a higher velocity and a lower temperature at any axial position. This explains the effect of the inlet stagnation pressure on the gas Mach number. Given an initial particle velocity, both the acceleration and the subsequent particle velocity should be increased due to the increase in the velocity difference between the gas medium and the particle. The increase in the gas velocity tends to increase the axial interval distance between neighboring particles, namely, to increase the degree of dispersion of the particles, and thus decrease the local particle volume fraction.

4.4 Effect of inlet stagnation temperature

Figure 12a–c shows the plots of the particle velocity v_p, gas Mach number M_g, and particle volume fraction φ for $\psi = 1.161$ at different inlet stagnation temperatures. It is found that the particle velocity increases faster, while the gas Mach number increases more slowly as the inlet stagnation temperature increases. However, for a constant particle mass loading, there is no clear dependency between the inlet stagnation temperature and the particle volume fraction. The increase in the inlet stagnation temperature, or the initial internal energy of the gaseous medium, means that more of the internal energy can be retained in the gas phase and meanwhile transformed into the gas kinetic energy during the process of the gaseous expansion. Consequently, the rate of decrease in the gas temperature is restricted, whereas the rate of increase in the gas velocity is promoted at the same time. Furthermore, the resulting increase in the local sound speed is more remarkable than that of the gas velocity. This explains the aforementioned effect of the inlet stagnation temperature on the gas Mach number. The increase in the gas velocity leads to the increase in the particle velocity because of the increased velocity difference and thus the increased gas flow force.
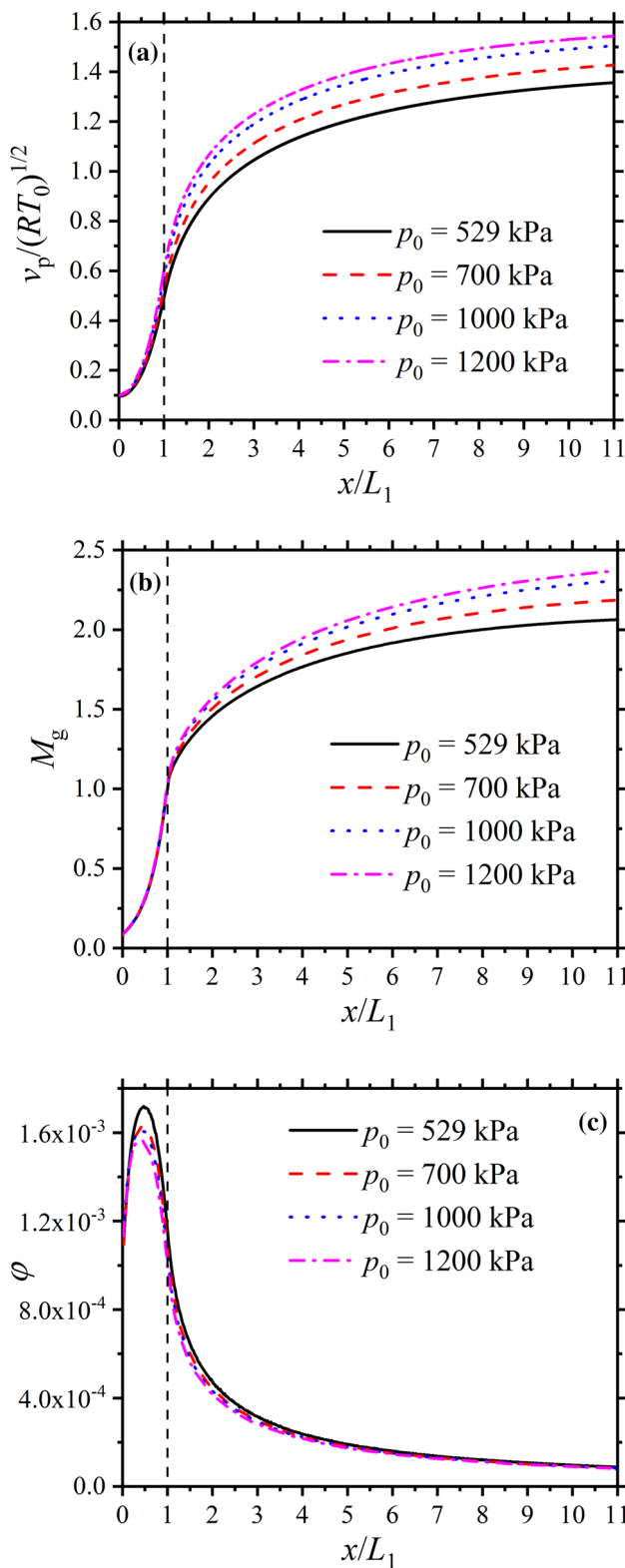
Fig. 11 Plots of **a** $v_p/(RT_0)^{1/2}$; **b** M_g; and **c** φ for $\psi = 1.161$ at different inlet stagnation pressures
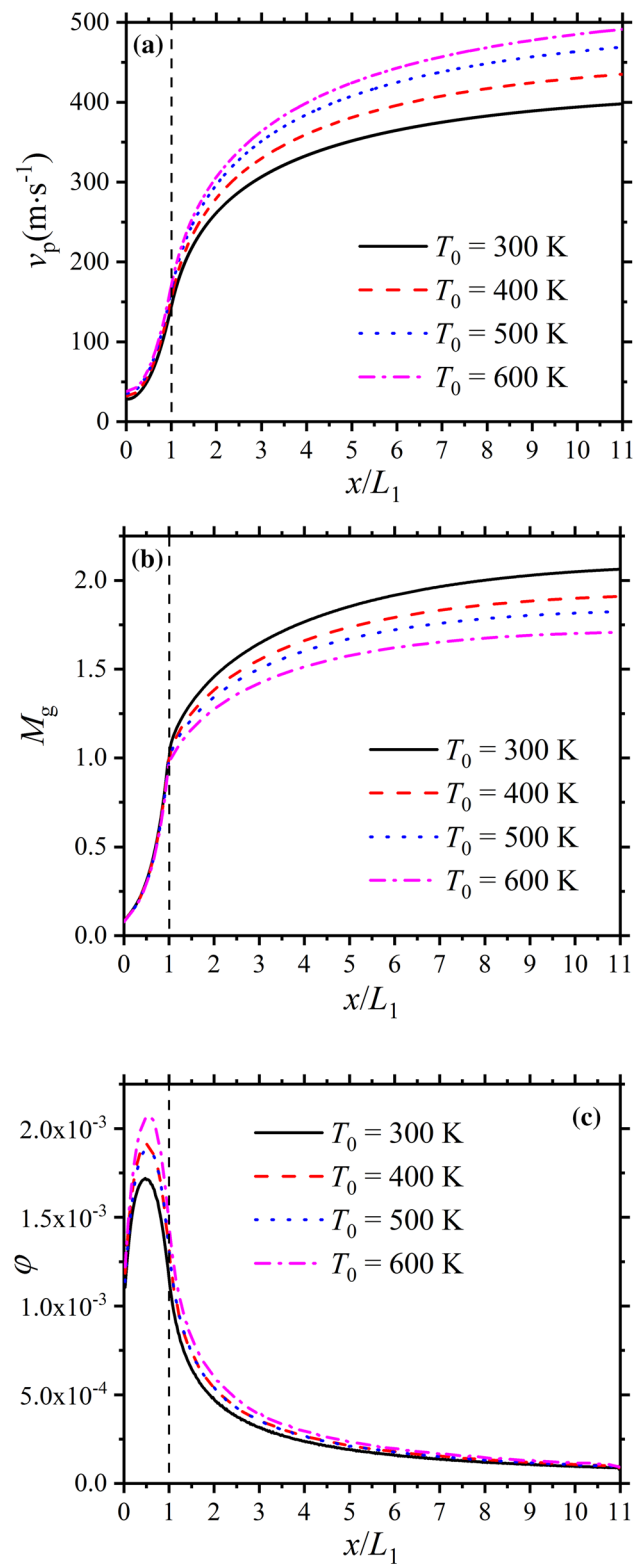
Fig. 12 Plots of **a** v_p; **b** M_g; and **c** φ for $\psi = 1.161$ at different inlet stagnation temperatures

Under a constant particle mass loading condition, the increase in the inlet stagnation temperature increases the gas velocity and particle mass flow rate simultaneously. As stated above, the increased gas velocity can promote the degree of dispersion of the particles. Namely, the greater gas velocity corresponds to the lower particle volume fraction. Compared with the gas velocity, the particle mass flow rate plays a completely opposite role on the local particle volume fraction. Neither the increased gas velocity nor the decreased particle mass flow rate can always dominate the effect on the particle volume fraction when the inlet stagnation temperature is increased. As a result, the influence of the inlet stagnation temperature on the variation of the particle volume fraction is quite complex. We can see from Fig. 12c that the two curves corresponding to $T_0 = 400$ K and 500 K intertwine with one another.

4.5 Effect of nozzle expansion angle

Figure 13a–c presents the plots of the particle velocity $v_p/(RT_0)^{1/2}$, gas Mach number M_g, and particle volume fraction φ at different nozzle expansion angles. It can be seen that the particle velocity and gas Mach number rise faster, and the particle volume fraction decreases with increasing expansion angle. The increase in the expansion angle directly increases the expansion effect of the gas medium in the divergent section. Consequently, the rate of decrease in the gas temperature and the rate of increase in the gas velocity are increased simultaneously. Thus, the increase in the gas Mach number is significantly promoted. The increase in the gas velocity leads to the increased particle velocity through the momentum exchange between the gas and particle two phases. The mass flow rates of particles corresponding to the expansion angles $\delta = 2.50°$, 3.00°, 3.44°, and 4.00° are within the range of 0.03760–0.03779 kg s^{-1}. The maximum relative deviation is only 0.51%. Nevertheless, the deviations of the gas and particle velocities caused by the change of expansion angle are remarkably greater. For example, the exit gas velocities corresponding to these expansion angles are 441.51–473.15 m s^{-1}, and meanwhile, the corresponding exit particle velocities are 384.88–402.38 m s^{-1}. The maximum relative deviations are 7.17% and 4.55%, respectively. Consequently, the variation of the particle volume fraction is mainly affected by the changes of the gas and particle velocities. In comparison, the effect of the change in the particle mass flow rate is relatively negligible. The increases in both the gas and particle velocities tend to decrease the local particle volume fraction. This explains the aforementioned effect of the increase in the expansion angle on the variation of the particle volume fraction.
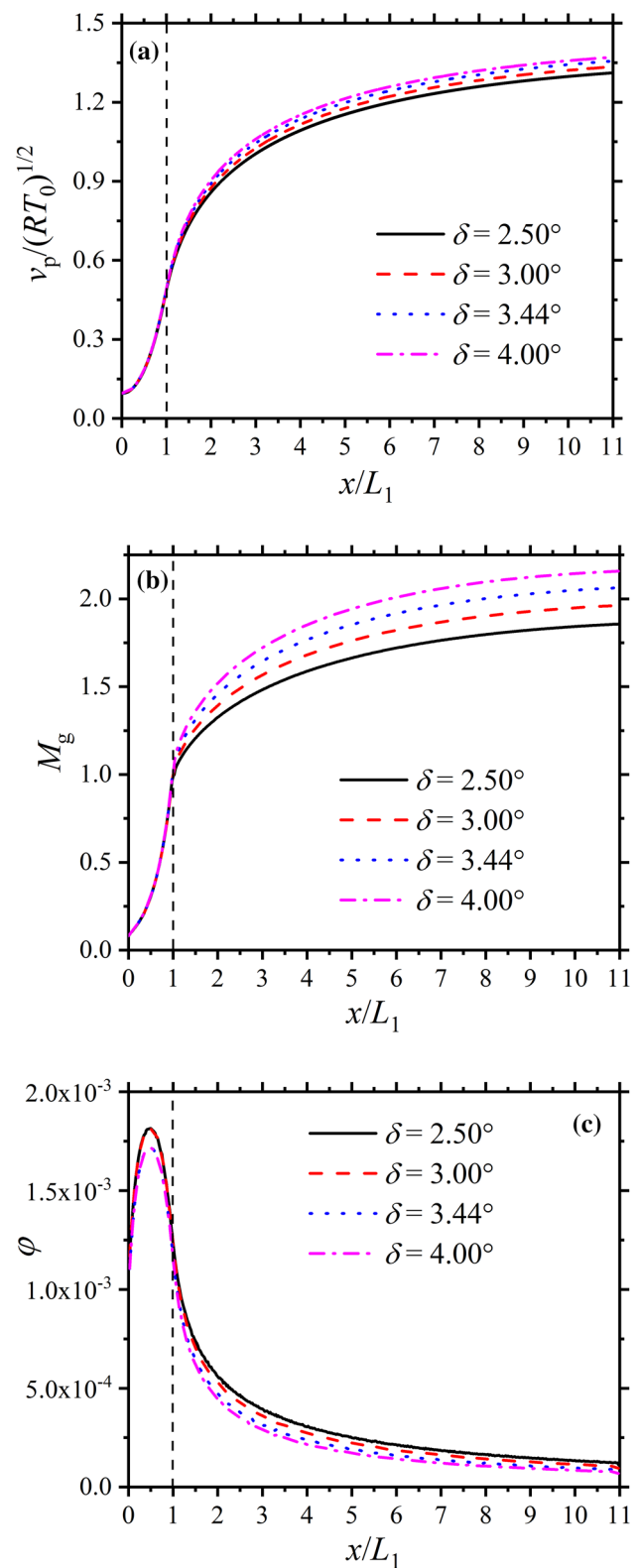

Fig. 13 Plots of **a** v_p; **b** T_p; and **c** φ for $\psi = 1.161$ at different nozzle expansion angles

5 Conclusions

In the present work, we first establish a gas-particle coupled quasi-one-dimensional model for particle-laden gas flows in the de Laval nozzles. Then, we create a set of uniformly high-order accurate, stable, and efficient numerically computational methods. Next, we calibrate the corrected turbulent boundary layer model and validate the numerical model against two experiments. Finally, we perform a series of numerical computations for a parametric study. The main conclusions are as follows.

Overall, the increase in the particle size suppresses the particle velocity, promotes the gas Mach number, and increases the particle volume fraction. An increase in the particle mass loading reduces the particle velocity and gas Mach number and increases the particle volume fraction. As the inlet stagnation pressure increases, particle velocity and gas Mach number are increased, while the particle volume fraction is decreased. The particle velocity increases, while the gas Mach number decreases with increasing inlet stagnation temperature. As the nozzle expansion angle increases, particle velocity and gas Mach number increase, while the local particle volume fraction decreases.

Appendix: Numerical methodology

Discretization methods for governing equations

In consideration of the prominently hyperbolic feature of the gas-phase conservation equations, a fifth-order WENO scheme [21] is employed to discretize the spatial derivative term of the flux vector (or convective term) on the left side of (1). However, it is necessary to conduct a characteristic splitting for the flux vector in advance. A modified Steger–Warming splitting method [18] is adopted in the present numerical model.

In order to make sure the spatial discretization for the gas-phase properties is at least third-order accurate, special treatments are required for grid nodes close to the nozzle inlet and exit boundaries. We combine a third-order upwind difference with a third-order upwind compact difference [18] to create the difference expressions for these nodes. Additionally, we adopt a simple third-order upwind difference approximation for the spatial derivatives such as the one of particle volume fraction in (19).
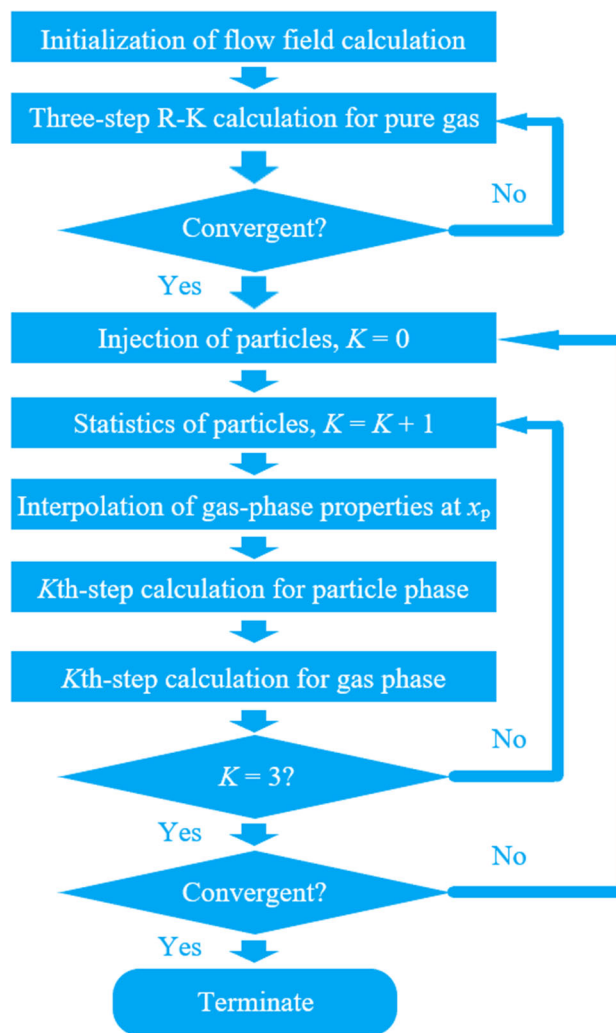

Fig. 14 Algorithmic flowchart

Shu and Osher's [27] three-step third-order total variation diminishing Runge–Kutta (R–K) scheme is used for the difference approximation of the time derivatives.

Interpolation of the gas properties at particle locations

When we perform the calculations for the particle phase, the information of the gas phase should be provided in advance. However, the solution of the gas phase only provides the information at grid nodes. Therefore, we introduce a cubic polynomial interpolation for the properties of the gas phase at the particle positions.

Computational procedure of flow fields

The procedure for the present computations of the gas-particle two-phase flow is as shown in Fig. 14. The con-

vergence criterion $E_r < \varepsilon_r$ is adopted, where the residual of mass flow rate of the gas is defined by

$$E_r = \max \left\{ \left| q_{mg}^{(n)} - q_{mg}^{(n-1)} \right| / q_{mg}^{(n)} \right\} \tag{31}$$

and the threshold value $\varepsilon_r = 10^{-5}$. For clarity, we also list the bullet points as follows:

1. Initialize the calculation with an isentropic gas flow.
2. Calculate f_{wf}, Q_w, and G_w at each node.
3. Calculate v_g, p, T_g, and ρ_g at the nozzle inlet.
4. Calculate ρ_g, v_g, e^*, e, T_g, and p at each node.
5. Repeat (2)–(4) until the three-step R–K calculation is finished at this time step.
6. Calculate E_r. If $E_r \geq \varepsilon_r$, turn back to (5). Otherwise (i.e., $E_r < \varepsilon_r$), if the current calculation is for gas-particle two-phase flow, terminate the calculation; if the current calculation is just for pure gas flow, proceed to the following steps.
7. Inject particles by allocating x_p, v_p, and T_p.
8. Reorder the new numbers for the remaining particles.
9. Calculate N_{JI}, φ, and α in each cell.
10. Calculate ρ_g, p, and T_g at particle locations.
11. Calculate f^{gp}, f^{pp}, and Q^{gp} for each particle.
12. Calculate v_p, x_p, and T_p for each particle.
13. Calculate G^{pg} and Q^{pg} in each cell, and turn back to (5).

References

1. Xu, T.X., Zhang, L.T., Xin, Y.: New dedusting concept of high temperature and high pressure gases. J. Xi'an Jiaotong Univ. **38**(7), 690–692, 745 (2004) (**in Chinese**). https://doi.org/10.3321/j.issn:0253-987X.2004.07.008
2. Gao, T.Y., Gong, J.Y., Wang, X.H.: Numerical and experimental study on a new separation device for gas–solid two-phase flows. Sep. Sci. Technol. **46**, 2456–2464 (2011). https://doi.org/10.1080/01496395.2011.611210
3. Hu, Z.M., Myong, R.S., Nguyen, A.T., Jiang, Z.L., Cho, T.H.: Numerical analysis of the flowfield in a supersonic coil with an interleaved jet configuration and its effect on the gain distribution. Eng. Appl. Comput. Fluid Mech. **1**(3), 207–215 (2007). https://doi.org/10.1080/19942060.2007.11015193
4. Guo, L., Yan, Y.Y., Maltson, J.D.: Performance of 2D scheme and different models in predicting flow turbulence and heat transfer through a supersonic turbine nozzle cascade. Int. J. Heat Mass Transf. **55**, 6757–6765 (2012). https://doi.org/10.1016/j.ijheatmasstransfer.2012.06.083
5. Yu, Y., Xu, J.L., Mo, J.W., Wang, M.T.: Principal parameters in flow separation patterns of over-expanded single expansion RAMP nozzle. Eng. Appl. Comput. Fluid Mech. **8**(2), 274–288 (2014). https://doi.org/10.1080/19942060.2014.11015513
6. Sudhan, K.H., Prasad, G.K., Kothurkar, N.K., Srikrishnan, A.R.: Studies on supersonic cold spray deposition of microparticles using a bell-type nozzle. Surf. Coat. Technol. **383**, 125244 (2020). https://doi.org/10.1016/j.surfcoat.2019.125244
7. Balachandar, S., Eaton, J.K.: Turbulent dispersed multiphase flow. Annu. Rev. Fluid Mech. **42**, 111–133 (2010). https://doi.org/10.1146/annurev.fluid.010908.165243
8. McGrath, T., Clair, J.S., Balachandar, S.: Modeling compressible multiphase flows with dispersed particles in both dense and dilute regimes. Shock Waves **2**, 1–12 (2017). https://doi.org/10.1007/s00193-017-0726-8
9. Bhattacharya, S., Lutfurakhmanov, A., Hoey, J.M., Swenson, O.F., Mahmud, Z., Akhatov, I.S.: Aerosol flow through a converging-diverging micro-nozzle. Nonlinear Eng. **2**, 103–112 (2013). https://doi.org/10.1515/nleng-2013-0020
10. Kudryavtsev, A., Shershnev, A., Rybdylova, O.: Numerical simulation of aerodynamic focusing of particles in supersonic micronozzles. Int. J. Multiph. Flow **114**, 207–218 (2019). https://doi.org/10.1016/j.ijmultiphaseflow.2019.03.009
11. Molleson, G.V., Stasenko, A.L.: Acceleration of microparticles in a gasdynamic facility with high expansion of flow. High Temp. **46**(1), 100–107 (2008). https://doi.org/10.1134/s10740-008-1014-1
12. Parmar, M., Haselbacher, A., Balachandar, S.: Improved drag correlation for spheres and application to shock-tube experiments. AIAA J. **48**(6), 1273–1276 (2010). https://doi.org/10.2514/1.J050161
13. Bailey, A., Starr, R.: Sphere drag at transonic speeds and high Reynolds numbers. AIAA J. **14**(11), 1631–1631 (1976). https://doi.org/10.2514/3.7262
14. Stewart, C., Balachandar, S., McGrath, T.P.: Soft-sphere simulations of a planar shock interaction with a granular bed. Phys. Rev. Fluids **3**, 034308 (2018). https://doi.org/10.1103/PhysRevFluids.3.034308
15. Harris, S.E., Crighton, D.G.: Solitons, solitary waves, and voidage disturbances in gas-fluidized beds. J. Fluid Mech. **266**, 243–276 (1994). https://doi.org/10.1017/S0022112094000996
16. Ling, Y., Wagner, J.L., Beresh, S.J., Kearney, S.P., Balachandar, S.: Interaction of a planar shock wave with a dense particle curtain: modeling and experiments. Phys. Fluids **24**, 113301 (2012). https://doi.org/10.1063/1.4768815
17. Luo, X., Wang, G., Olivier, H.: Parametric investigation of particle acceleration in high enthalpy conical nozzle flows for coating applications. Shock Waves **17**, 351–362 (2008). https://doi.org/10.1007/s00193-007-0116-8
18. Fu, D.X., Ma, Y.W., Li, X.L., Wang, Q.: Direct Numerical Simulation of Compressible Turbulent Flows, pp. 60–184. Science Press, Beijing (2010) (**in Chinese**)
19. Shershnev, A., Kudryavtsev, A.: Kinetic simulation of near field of plume exhausting from a plane micronozzle. Microfluid. Nanofluid. **19**, 105–115 (2015). https://doi.org/10.1007/s10404-015-1553-9
20. Li, Z.J., Wang, H., Chen, J.W.: Ground effects on the hypervelocity jet flow and the stability of projectile. Eng. Appl. Comput. Fluid Mech. **12**(1), 375–384 (2018). https://doi.org/10.1080/19942060.2018.1445034
21. Jiang, G.S., Shu, C.W.: Efficient implementation of weighted ENO schemes. J. Comput. Phys. **126**, 202–228 (1996). https://doi.org/10.1006/jcph.1996.0130
22. Jones, J.B., Dugan, R.E.: Engineering Thermodynamics. Prentice Hall Inc., New Jersey (1996)
23. Snider, D.M., O'Rourke, P.J., Andrews, M.J.: Sediment flow in inclined vessels calculated using a multiphase particle-in-cell model for dense particle flows. Int. J. Multiph. Flow **24**, 1359–1382 (1998). https://doi.org/10.1016/s0301-9322(98)00030-5
24. Drake, R.M.: Discussion on G.C. Vliet and G. Leppert: forced convection heat transfer from an isothermal sphere to water. J. Heat Transf. Trans. ASME **83**, 170–172 (1961). https://doi.org/10.1115/1.3680507

25. Meyer, M., Caruso, F., Lupoi, R.: Particle velocity and dispersion of high Stokes number particles by PTV measurements inside a transparent supersonic cold spray nozzle. Int. J. Multiph. Flow **106**, 296–310 (2018). https://doi.org/10.1016/j.ijmultiphaseflow.2018.05.018

26. Fang, D.Y.: Two-Phase Flow Dynamics, National University of Defense Technology Press, Changsha, pp. 153–240 (1988) (**in Chinese**)

27. Shu, C.W., Osher, S.: Efficient implementation of essentially non-oscillatory shock-capturing schemes. J. Comput. Phys. **77**(2), 439–471 (1988). https://doi.org/10.1016/0021-9991(88)90177-5